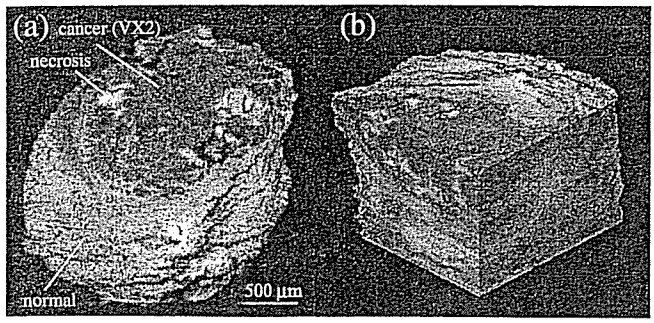

Fig. 8. Rabbit liver tissue with VX2 cancer examined by phase tomography with 0.1 nm X-rays. Cancerous lesion was clearly differentiated from normal tissue in (a), and necrosis in the tumor was revealed. (b) is a three-dimensional rendering view of a part of reconstructed data.

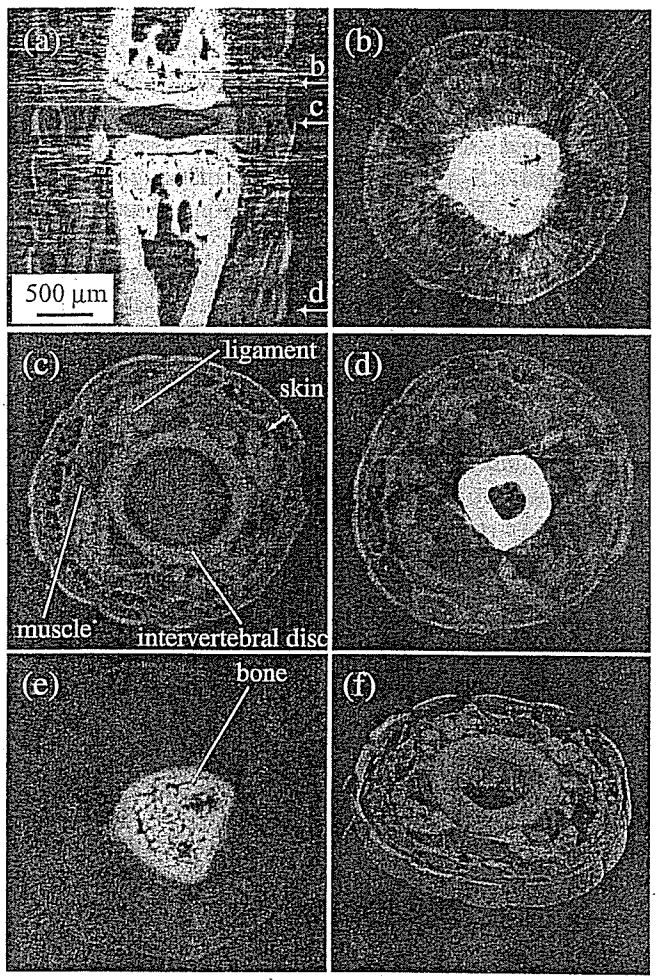

Fig. 9. Mouse tail observed by phase tomography with 0.07 nm X-rays. In the sagital image (a), the positions of the axial images (b), (c), and (d) are indicated by arrows. The grayscale of (b)–(d) corresponds to the refractive index difference ranging from 0 to 2×10^{-7}. A redrawing of (b) with a grayscale from 0 to 7×10^{-7} is shown in (e), where a trabecular structure of the bone is shown. (f) is a three-dimensional rendering view of a portion containing an intervertebral disc.

A piece of rabbit liver with cancer (VX2) was first examined using 0.1 nm X-rays. A cancerous lesion depicted with a lower grayscale value was clearly differentiated from a normal tissue as shown in Fig. 8. Furthermore, necrosis was detected as bright areas in the cancerous lesion. The grayscale corresponds to the refractive index difference ranging from 0 to 1.1×10^{-7}. This feature is comparable to the result obtained by phase tomography using a Mach–Zehnder type crystal X-ray interferometer.[38]

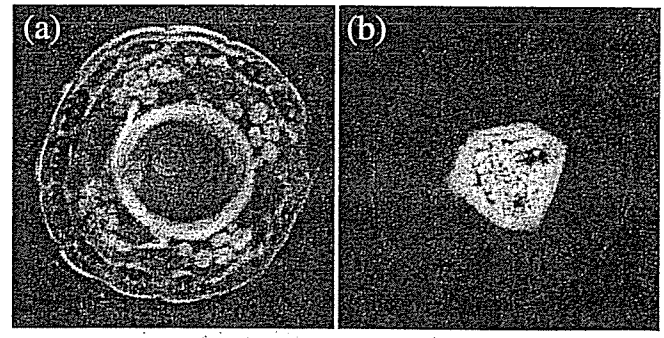

Fig. 10. Mouse tail identical to sample shown in Fig. 9, observed by phase tomography with 0.04 nm X-rays. The slice positions of (a) and (b) correspond to those of Figs. 9(c) and 9(e). The grayscales of (a) and (b) correspond to the refractive index difference ranging from 0 to 6×10^{-8} and to 2×10^{-7}, respectively.

XTI is available for a sample containing bone tissue, while phase tomography with a crystal X-ray interferometer is not suitable for such a sample because interference fringes that are too fine to resolve are generated by bones. Figure 9 shows a result obtained for a mouse tail using 0.07 nm X-rays. The arrows in the sagital image [Fig. 9(a)] indicate the positions of axial images shown in Figs. 9(b)–9(d). Soft tissue structures, such as muscle, ligament, skin, and intervertebral disc (cartilage), were depicted with bones in the same view although the bones generated some artifacts. The bones in these views are saturated, but a trabecular structure was depicted by changing the grayscale, as shown in Fig. 9(e).

It should be noted that the contrast of the bones does not include the contribution of absorption, which was eliminated by the operation in eq. (16). If the information of absorption is needed, it can be obtained by calculating amplitude instead of the argument as in the right term of eq. (16).

The X-ray Talbot interferometer functioned using 0.04 nm X-rays, as suggested by the result shown in Fig. 7. Therefore, the mouse tail was observed at this wavelength, as shown in Fig. 10, whose axial positions corresponded to those of Figs. 9(c) and 9(e). Although Fig. 10 seems to be slightly noisier than Fig. 9, one reason for which is the lower visibility of moiré fringes at 0.04 nm, this result fully suggests that our X-ray Talbot interferometer is available for X-ray phase tomography at this energy.

4. Discussion

4.1 Resolution

The spatial resolution of an image obtained by XTI is limited by the period of the grating. Including other factors such as the resolution of the image detector and noise, actual spatial resolution is determined. We evaluated spatial resolution on the basis of the average full width at half maximum (FWHM) of differential contrast profiles across boundaries between the sample and surrounding medium (formalin) in phase tomograms. From Figs. 8 and 10, 14 and 16 μm were obtained, respectively. To improve spatial resolution, gratings of a smaller period are necessary.

Contrast resolution, which describes the high sensitivity

of X-ray phase imaging, was evaluated on the basis of the standard deviation in the tomograms at the region of the surrounding formalin. In the X-ray energy region, the refractive index decrement δ, which phase tomography reveals as explained, is approximately given by

$$\delta = \frac{r_e \lambda^2}{2\pi} \rho, \tag{21}$$

where r_e is the classical electron radius and ρ is the electron density. This implies that the contrast in phase tomograms corresponds to a map of electron density. Furthermore, particularly for materials consisting of light elements, electron density is approximately proportional to mass density. Therefore, a phase tomogram is considered to be a mass density map. The standard deviation of voxel values in a part of the surrounding formalin region of Fig. 8 was 1.9×10^{-9}. The detection limit of density deviation was therefore estimated to be 1.3 mg/cm^3 because the δ of formalin, which is almost the same as that of water,[39] is 1.5×10^{-6} for 0.1 nm X-rays. Similarly, we obtained 2.2 and 5.9 mg/cm^3 for 0.07 and 0.04 nm X-rays, respectively, from Figs. 9 and 10. Thus, the sensitivity to density deviation is better with X-rays of longer wavelengths. This result is consistent with the fact that δ is proportional to the square of λ [eq. (21)].

However, it should be emphasized that errors in the unwrapping are reduced with decreasing wavelength. This is because a too strong refraction is suppressed moderately, therefore, a too rapid change in resultant φ_x is reduced. For samples containing high-density regions such as bone, the use of higher energy X-rays is significant in this sense.

4.2 *Requirements for X-ray beam quality*

The experiments reported in this paper were performed with synchrotron radiation assuming plane-wave monochromatic X-rays. However, as mentioned in the Introduction, XTI functions in principle with spherical-wave (cone-beam) X-rays with a broad energy band because of the use of grating optics. Here, the performance of XTI is discussed when polychromatic X-rays are used.

The change in φ_x caused by the spectral change $\Delta\lambda$ is given using eqs. (9), (12), and (21) by

$$\Delta\varphi_x = \Delta\lambda \frac{r_e \lambda}{\pi} \int \frac{\partial \rho}{\partial x} dz. \tag{22}$$

Because the positions of moiré fringes are determined by the maximum of $\cos(2\pi z_T \varphi_x / d)$, as suggested in eq. (11), the spectral change moves moiré fringes in proportion to

$$\frac{2\pi}{d} z_T \Delta\varphi_x = 2 m r_e \Delta\lambda d \int \frac{\partial \rho}{\partial x} dz. \tag{23}$$

As a result, a finite band width causes a decrease in the visibility of moiré fringes. An acceptable band width so that moiré fringes are not smeared out is evaluated using

$$2 m r_e \Delta\lambda d \int \frac{\partial \rho}{\partial x} dz < \frac{\pi}{2}. \tag{24}$$

Here, let us consider a case of detecting an air bubble in water. We assume that the pixel size of an image detector is d, which is the same as the period of the grating, since a smaller pixel size is meaningless because the spatial resolution of XTI is limited by d according to its principle. Then, the maximum gradient that would be measured with a discrete sampling is $\sqrt{D/d}$, where D is the diameter of the air bubble, and eq. (24) is rewritten as

$$4 m r_e \Delta\lambda d \rho \sqrt{\frac{D}{d}} < \frac{\pi}{2}. \tag{25}$$

Using the parameters used in this study ($d = 8\,\mu$m, $m = 1/2$) and $\rho = 3.3 \times 10^{29}$ m^{-3} for water,

$$\Delta\lambda \sqrt{D} < 2.9 \times 10^{-13}, \tag{26}$$

where $\Delta\lambda$ and D are given with the unit of meter. This implies that $\Delta\lambda$ can be broaden up to 29 pm without smearing out an air bubble 100 μm in diameter in water. Thus, X-rays with a bandwidth $\Delta\lambda/\lambda \sim 0.1$ are certainly available. However, this result suggests at the same time that a narrower band should be selected so as to satisfy eq. (24) when a thicker object is observed.

The above discussion was presented neglecting the degradation of the performance of XTI by band width. Because z_T is inversely proportional to λ, the visibility of moiré fringes should be worse in the case of using polychromatic X-rays than in the case of using monochromatic X-rays. The contrast of the self-image has maxima along z every d^2/λ, as suggested by eq. (6). Assuming that the change in z_T induced by the spectral change of $\pm\Delta\lambda$ is smaller than $(1/4)(d^2/\bar{\lambda})$, a condition that moiré fringes are visible would be given by

$$\frac{\Delta\lambda}{\bar{\lambda}} < \frac{1}{8}, \tag{27}$$

where $\bar{\lambda}$ is the central wavelength. Thus, XTI is tolerant of the broadness of X-ray spectrum.

The above result implies that XTI does not require temporal coherency for its operation. However, requirement for spatial coherency should be noted. From the viewpoint of geometrical optics, the Talbot effect is understood as a result of interference mainly between neighboring diffraction orders generated by the grating. The angular difference between two beams of neighboring orders is λ/d, and therefore an interference fringe pattern, or self-image, with a period d is formed. Because the two beams are spatially separated by $\lambda z_T/d = md$ at $z = z_T$, the spatial coherence length should be approximately larger than md, in the case of presented study $d/2$.

In general, the spatial coherence length L is defined by

$$L = \frac{\lambda R}{2\pi\sigma_x}, \tag{28}$$

at the distance R from an X-ray source with a Gaussian intensity distribution $\exp(-x^2/2\sigma_x^2)$. Figure 11 shows the fringe visibilities of the self-image of a $\pi/2$ phase grating at $z = d^2/2\lambda$ as a function of L/d. The visibility curve is independent of λ, and when the coherence length is larger than one-half of the grating period, a self-image with a visibility of more than 0.7 is produced, which is enough for phase imaging provided the pattern of the second grating is sufficiently thick. It is noteworthy that a visibility of 0.4 is attained even $L/d \approx 1/3$.

4.3 *Prospects*

As presented, phase imaging at 0.04 nm was successful,

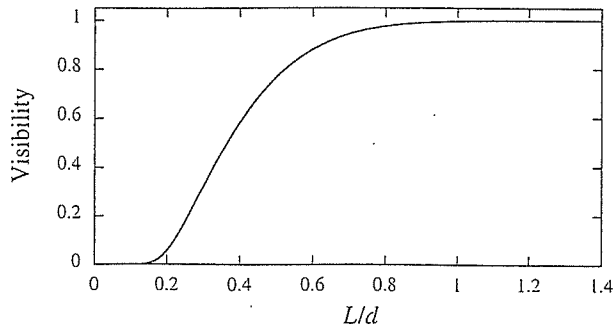

Fig. 11. Visibility of self-image of $\pi/2$ phase grating at $z = d^2/2\lambda$ as function of ratio of coherence length (L) and period of grating (d).

but it is of course necessary to fabricate a thicker pattern to attain a better imaging quality at this or a higher-energy region. At the same time, the area of the grating should be increased for practical imaging applications. The period of the gratings is also preferred to be shortened because the system can be compact and the requirement for spatial coherency is moderated. We consider that such developments are possible by improving the fabrication technology used in this study.

Although this study demonstrated XTI with synchrotron radiation, which can be assumed to be plane-wave X-rays, the development of cone-beam XTI with a compact X-ray source is significant for practical applications. The principle of XTI is common in cone-beam XTI, aside from some modifications. When a spherical wave is used, the positions of self-imaging given by eq. (6) for the plane-wave case must be replaced by

$$z_T = \frac{md_1^2R}{R\lambda - md_1^2}, \tag{29}$$

where R is the distance between the source and the first grating with a period d_1.[40] The period d_2 of the second grating is different from d_1 and has a relation

$$d_1 : d_2 = R : (R + z_T). \tag{30}$$

Although the use of spherical gratings would be ideal in this case, flat gratings are also available for XTI with a spherical wave, provided that R is sufficiently larger than the size of the field of view, theoretical considerations on which will be described elsewhere.[41]

As for an image detector, XTI does not require a spatial resolution as high as that for resolving the self-image. Therefore, a variety of X-ray image detectors should be compatible with XTI. Here, it should be noted that an image detector in combination with the two gratings can be considered as a phase-sensitive image detector. In this sense, XTI is a breakthrough for the development of the first X-ray wavefront sensor.

Because XTI is operated with a cone beam with a broad energy band, its instrumentation outside synchrotron radiation facilities is highly expected. What types of X-ray source are available for cone-beam XTI? Normal X-ray generators used in hospitals are not available because of the lack of spatial coherency. The source size and source-grating distance must be selected to produce a spatial coherence length enough to generate the Talbot effect. It is therefore preferable to use a small source at a position far from it [see eq. (28)]. For instance, if $d_1 = 5\,\mu\text{m}$, $\lambda = 0.04\,\text{nm}$, and $\sigma_x = 5\,\mu\text{m}$ (FWHM of the source size is about $12\,\mu\text{m}$), then R should be larger than 2 m. At the same time, a sufficient flux is needed for imaging with a practical exposure time. These two requirements are contrary to each other.

Assuming that 10^3 photons/s are needed per $50\,\mu\text{m}$ pixel for phase imaging and that a field of view of $100 \times 100\,\text{mm}^2$ is covered with an array of pixels, an X-ray source emitting 2×10^{13} photons/s in the entire solid angle is required under the above conditions with respect to σ_x and R. Even taking into account the bandwidth available for XTI discussed above, the wattage of such an X-ray source should be over 100 W, which is much higher than that of commercially available microfocus X-ray generators. Although the requirement for X-ray sources is moderated using XTI as discussed above, we need to make an effort as well to develop a microfocus X-ray source with an improved brightness for practical phase imaging by XTI.

5. Conclusions

The principle of X-ray phase imaging and phase tomography with XTI was described, and successful biological imaging results with synchrotron radiation were presented. The key for the construction of an X-ray Talbot interferometer is the fabrication of an amplitude grating, because a high-aspect-ratio pattern must be formed. We fabricated a gold grating by X-ray lithography and electroplating. The X-ray Talbot interferometer with the gold grating functioned with synchrotron X-rays down to 0.04 nm wavelength. Provided that a grating with a higher aspect ratio and a wider effective area is fabricated, XTI is an attractive candidate for practical X-ray phase imaging, such as that for clinical diagnoses, because XTI has an advantage in that cone-beam X-rays of a broad energy band are available, allowing its compatibility with a compact X-ray source.

Acknowledgements

We appreciate the biological samples provided by Drs. J. Wu and T. Takeda (University of Tsukuba, Japan), the use of which was approved by the Medical Committee for the Use of Animals in Research of University of Tsukuba. The experiments using synchrotron radiation were performed under the approval of SPring-8 committee 2005A0326-NM-np. This study was financially supported by the project "Development of System and Technology for Advanced Measurement and Analysis" of Japan Science and Technology Agency (JST).

1) R. Fitzgerald: Phys. Today **53** (2000) 23.
2) A. Momose: Jpn. J. Appl. Phys. **44** (2005) 6355.
3) A. Momose and J. Fukuda: Med. Phys. **22** (1995) 375.
4) U. Bonse and M. Hart: Appl. Phys. Lett. **6** (1965) 155.
5) M. Ando and S. Hosoya: Proc. 6th Int. Conf. X-ray Optics and Microanalysis, Tokyo, 1972, p. 63.
6) A. Momose: Nucl. Instrum. Methods Phys. Res., Sect. A **352** (1995) 622.
7) F. Beckmann, U. Bonse, F. Busch and O. Günnewig: J. Comput. Assist. Tomogr. **21** (1997) 539.
8) V. A. Somenkov, A. K. Tkalich and S. Sh. Shil'shtein: Sov. Phys. Tech. Phys. **36** (1991) 1309.
9) T. J. Davis, D. Gao, T. E. Gureyev, A. W. Stevenson and S. W. Wilkins: Nature **373** (1995) 595.

10) V. N. Ingal and E. A. Beliaevskaya: J. Phys. D **28** (1995) 2314.
11) D. Chapman, W. Thomlinson, R. E. Johnston, D. Washburn, E. Pisano, N. Gmür, Z. Zhong, R. Menk, F. Arfelli and D. Sayers: Phys. Med. Biol. **42** (1997) 2015.
12) A. Snigirev, I. Snigireva, V. Kohn, S. Kuznetsov and I. Schelokov: Rev. Sci. Instrum. **66** (1995) 5486.
13) K. A. Nugent, T. E. Gureyev, D. F. Cookson, D. Paganin and Z. Barnea: Phys. Rev. Lett. **77** (1996) 2961.
14) S. W. Wilkins, T. E. Gureyev, D. Gao, A. Pogany and A. W. Stevenson: Nature **384** (1996) 335.
15) P. Cloetens, W. Ludwig, J. Baruchel, D. Van Dyck, J. Van Landuyt, J. P. Guigay and M. Schlenker: Appl. Phys. Lett. **75** (1999) 2912.
16) F. A. Dilmanian, Z. Zhong, B. Ren, X. Y. Wu, L. D. Chapman, I. Orion and W. C. Thomlinson: Phys. Med. Biol. **45** (2000) 933.
17) I. Koyama, Y. Hamaishi and A. Momose: AIP Conf. Proc. **705** (2004) 1283.
18) A. Maksimenko, M. Ando, H. Sugiyama and T. Yuasa: Appl. Phys. Lett. **86** (2005) 124105.
19) I. Koyama, A. Momose, J. Wu, Thet Thet Lwin and T. Takeda: Jpn. J. Appl. Phys. **44** (2005) 8219.
20) Konica Minolta Technol. Rep. **2** (2005) 30 [in Japanese].
21) C. David, B. Nöhammer, H. H. Solak and E. Ziegler: Appl. Phys. Lett. **81** (2002) 3287.
22) A. Momose, S. Kawamoto, I. Koyama, Y. Hamaishi, K. Takai and Y. Suzuki: Jpn. J. Appl. Phys. **42** (2003) L866.
23) A. Momose, S. Kawamoto, I. Koyama and Y. Suzuki: Proc. SPIE **5535** (2004) 352.
24) T. Weitkamp, B. Nöhammer, A. Diaz, C. David and E. Ziegler: Appl. Phys. Lett. **86** (2005) 054101.
25) T. Weitkamp, A. Daiz, C. David, F. Pfeiffer, M. Stampanoni, P. Cloetens and E. Ziegler: Opt. Express **13** (2005) 6296.
26) S. Yokozeki and T. Suzuki: Appl. Opt. **10** (1971) 1575.
27) A. W. Lohmann and D. E. Silva: Opt. Commun. **2** (1971) 413.
28) A. Momose and S. Kawamoto: Jpn. J. Appl. Phys. **45** (2006) 314.
29) M. Matsumoto, K. Takiguchi, M. Tanaka, Y. Hunabiki, H. Takeda, A. Momose, Y. Utsumi and T Hattori: High Aspect Ratio Micro Structure Technology Workshop, 2005, p. 22.
30) P. Cloetens, J. P. Guigay, C. De Martino, J. Baruchel and M. Schlenker: Opt. Lett. **22** (1997) 1059.
31) H. F. Talbot: Philos. Mag. **9** (1836) 401.
32) J. P. Guigay: Opt. Acta **18** (1971) 677.
33) M. Born and E. Wolf: *Principle of Optics* (Pergamon Press, Oxford, 1980) p. 508.
34) J. H. Bruning, D. R. Herriott, J. E. Gallagher, D. P. Rosenfeld, A. D. White and D. J. Brangaccio: Appl. Opt. **13** (1974) 2693.
35) K. A. Stetson and W. R. Brohinsky: Appl. Opt. **24** (1985) 3631.
36) J. M. Huntley: Appl. Opt. **28** (1989) 3268.
37) G. W. Faris and R. L. Byer: Appl. Opt. **27** (1988) 5202.
38) A. Momose, T. Takeda, Y. Itai and K. Hirano: Nat. Med. **2** (1996) 473.
39) A. Momose, T. Takeda and Y. Itai: unpublished.
40) K. Patorski: *Progress in Optics* (Elsevier, Amsterdam, 1989) Vol. 27.
41) W. Yashiro and A. Momose: in preparation.

Biomedical Imaging by Talbot-Type X-Ray Phase Tomography

Atsushi Momose[a], Wataru Yashiro[a], Masafumi Moritake[a], Yoshihiro Takeda[b], Kentaro Uesugi[c], Akihisa Takeuchi[c], Yoshio Suzuki[c], Makoto Tanaka[d], and Tadashi Hattori[d]

[a]Department of Advanced Materials Science, Graduate School of Frontier Sciences, The University of Tokyo, 5-1-5 Kashiwanoha, Kashiwa, Chiba 277-8651, Japan;
[b]Graduate School of Pure and Applied Sciences, University of Tsukuba, 1-1-1 Tennodai, Tsukuba, Ibaraki 305-8573, Japan;
[c]SPring-8/JASRI, 1-1-1, Kouto, Sayo, Hyogo 679-5198 Japan;
[d]Laboratory of Advanced Science and Technology for Industry, University of Hyogo, 3-1-2 Kouto, Kamigori, Hyogo 678-1205, Japan

ABSTRACT

An X-ray Talbot interferometer for X-ray phase imaging and tomography was constructed using an amplitude grating of a gold pattern 8 μm in pitch and 30 μm in height developed by X-ray lithography and gold electroplating. The effective area of the grating was 20 mm $\times$ 20 mm, and was fully illuminated by synchrotron radiation at beamline 20XU, SPring-8, Japan. Almost whole body of a fish 3 cm in length was observed by phase tomography. Resulting images obtained with 0.07 nm and 0.045 nm X-rays revealed organs with bones in the same view successfully. A preliminary result of the combination with an X-ray imaging microscope is also presented, which was attempted to attain a higher spatial resolution. Finally, prospects of the compatibility with a conventional X-ray generator are discussed for practical applications such as clinical diagnoses.

Keywords: Phase, Imaging, Tomography, Talbot effect, Talbot interferometer, Grating

1. INTRODUCTION

Recently, phase differential X-ray interferometry using X-ray transmission gratings has been attracting attentions as a novel phase-sensitive X-ray imaging method.[1–4] A contrast corresponding to the wavefront inclination caused by the X-ray refraction at a sample can be sensed. Its principle is the same as that of optical Talbot interferometry[5,6] that aligns two transmission gratings on an optical axis. The first grating causes the fractional Talbot effect; that is, a periodic intensity pattern, which we call as a 'self-image' in this paper, is formed at a specific distance from the grating determined by the pitch of the gratings and X-ray wavelength. When a phase object is placed in the beam path, the refraction at the sample reflects on the deformation of the self-image. The Talbot interferometer generate a moiré pattern by placing an amplitude grating, whose pitch is almost the same as the average period of the self-image, at the position of the self-image, as shown in Fig. 1(a).

Not only the generation of a phase-sensitive contrast but also quantitative measurement of the wavefront inclination, in other words a differential phase map, can be performed with an X-ray Talbot interferometer, allowing X-ray phase tomography. In this paper, we report a biological imaging result obtained using synchrotron radiation, including technical progress made since the previous report.[7] Because of using grating optics, X-ray Talbot interferometry has an attractive advantage that cone-beam and/or polychromatic X-rays are available. It is therefore possible to combine an X-ray Talbot interferometer with an X-ray imaging microscope. A preliminary experiment of Talbot-type phase-sensitive X-ray microscopy is also presented. Finally, the compatibility of X-ray Talbot interferometry with a conventional X-ray source for practical applications outside synchrotron facilities are discussed.

A.M.: E-mail: momose@exp.t.u-tokyo.ac.jp

Developments in X-Ray Tomography V, edited by Ulrich Bonse,
Proc. of SPIE Vol. 6318, 63180T, (2006) · 1605-7422/06/$15 · doi: 10.1117/12.678443

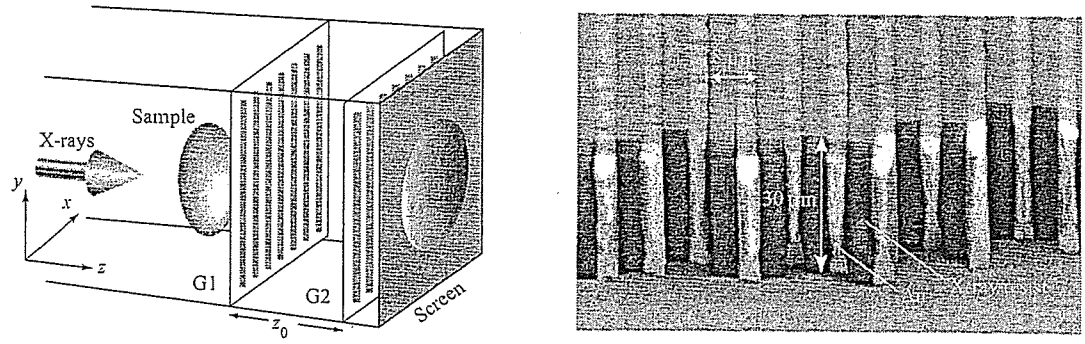

(a) (b)

Figure 1. Configuration of X-ray Talbot interferometer (a), where phase grating (G1) and amplitude grating (G2), whose SEM image is shown in (b), are aligned in line along X-ray axis.

2. METHOD

2.1. X-ray Gratings

An X-ray absorption grating is the key optical element in the successful operation of an X-ray Talbot interferometer. The visibility of moiré fringes is determined by the thickness of the grating pattern. We selected gold as a material of the pattern because of its high absorption coefficient and fabrication convenience. Nevertheless, a thickness of several tens of microns is required to block X-rays sufficiently. For instance, roughly 10 μm is needed at 20 keV, 30 μm at 30 keV, and 60 μm at 40 keV. On the other hand, the pitch of the grating should be comparable to the spatial coherent length of incident X-rays, which is in general of the order of microns. It is not straightforward to fabricate such a pattern of a high aspect ratio with conventional lithographic techniques. We have therefore attempted at fabricating X-ray amplitude gratings by X-ray lithography and gold electroplating.

The synchrotron radiation beamline 11 of NewSUBARU, Japan, which is dedicated to lithographie galvanoformung abformung (LIGA) fabrication, was used. A 30 μm X-ray resist film (MAX001, Nagase ChemteX) was spin-coated on a 200-μm Si wafer with a 0.25-μm Ti layer, and then a 4-μm L&S resist pattern (8 μm pitch) was fabricated by X-ray exposure. Gold lines were formed by electroplating between resist lines, which were left after the electroplating to support the gold lines (Fig. 1(b)). The effect of absorption by the X-ray resist is negligible. The height of the gold lines was nearly 30 μm, and the effective area of the grating was 20 × 20 mm^2.[8]

2.2. Tomographic Reconstruction

An X-ray Talbot interferometer consists of a phase grating (G1), an amplitude grating (G2) and an image detector. The spacing between the gratings is set so that the fractional Talbot effect by G1 occurs at the position of G2; that is, a self-image with a period corresponding to the pitch of G1 is formed on G2. When a phase object is placed in front of G1 or between G1 and G2, the self-image is deformed owing to the X-ray refraction at the object. When the pitch of G2 is almost the same as the pitch of the self-image, a moiré pattern is observed by an image detector placed just behind G2.

With plane-wave illumination, the self-image $I(x, y, z)$ formed by a grating is given by

$$I(x,y,z) = \left| \sum_n a_n \exp\left(-\pi i \lambda z \frac{n^2}{d^2}\right) \exp\left(2\pi i \frac{nx}{d}\right) \right|^2 \tag{1}$$

under a paraxial approximation, where d, λ, and a_n are the pitch of the grating, X-ray wavelength, and the coefficient of the Fourier series expansion of the complex transmission function of the grating, respectively. Here, the X-ray optical axis is parallel to the z axis, and the line pattern of the gratings is parallel to the y axis.

When a phase object that causes a phase shift $\Phi(x,y)$ is placed close to G1 ($z=0$), the phase of the n-th order diffraction by G1 is given by

$$\Phi\left(x-\frac{n\lambda z}{d},y\right)\approx\Phi(x,y)-\frac{n\lambda z}{d}\frac{\partial\Phi(x,y)}{\partial x} \tag{2}$$

with geometrical consideration. Equation (1) is therefore rewritten as

$$\begin{aligned} I(x,y,z) &= \left|\sum_n a_n\exp\left(-\pi i\lambda z\frac{n^2}{d^2}\right)\exp\left[i\left\{2\pi\frac{nx}{d}+\Phi\left(x-\frac{n\lambda z}{d},y\right)\right\}\right]\right|^2, \\ &\approx \sum_n b_n(z)\exp\left[2\pi i\frac{n}{d}\left(x-z\varphi(x,y)\right)\right], \end{aligned} \tag{3}$$

where

$$\varphi(x,y)=\frac{\lambda}{2\pi}\frac{\partial\Phi(x,y)}{\partial x}, \tag{4}$$

and $b_n(z)$ is given by

$$b_n(z)=\sum_{n'}\beta_{n+n'}\beta^*_{n'}, \qquad \beta_n\equiv a_n\exp\left(-\pi i\lambda z\frac{n^2}{d^2}\right). \tag{5}$$

It is known that 100% visibility is attained in principle when a self-image is observed at

$$z=d^2/2\lambda \tag{6}$$

with a $\pi/2$ phase grating.[9]

Giving the transmission function of G2, which has a pitch the same as the average period of $I(x,y,z)$, with

$$T(x,y)=\sum_n t_n\exp\left(2\pi i\frac{nx}{d}\right), \tag{7}$$

a moiré pattern

$$\begin{aligned} M(x,y,z) &= I(x,y,z)\times T(x+\chi,y) \\ &= \sum_n b_n(z)t_n\exp\left\{2\pi i\frac{n}{d}\left(z\varphi(x,y)+\chi\right)\right\} \end{aligned} \tag{8}$$

is observed. χ is the displacement of G2 in the x direction, and this freedom can be used for the quantitative measurement of $\varphi(x,y)$ by the fringe scanning method; that is,

$$2\pi\frac{z}{d}\varphi(x,y)\approx\arg\left[\sum_k^M M_k(x,y,z)\exp\left(-2\pi i\frac{k}{M}\right)\right], \tag{9}$$

where $M_k(x,y,z)$ is the moiré pattern when $\chi=kd/M$ ($k=1,2,\cdots,M$). Strictly, higher orders in eq. (8) cause error in the determination of $\varphi(x,y)$ with eq. (9). If a sufficiently large number is selected for M, such an error can be reduced.[4,7,10]

The input data of phase tomography is normally $\Phi(x,y,\theta)$, which is the projection of the refractive index difference δ; that is,

$$\Phi(x,y,\theta)=\frac{2\pi}{\lambda}\int\delta(X,y,Z)dz, \tag{10}$$

where (X,y,Z) is the coordinate fixed with the object, and θ is the angle between the x and X axes. In the present case, we measure $\varphi(x,y)$ that satisfies

$$\varphi(x,y,\theta)=\int\frac{\partial\delta(X,y,Z)}{\partial x}dz. \tag{11}$$

In order to follow the process based on eq. (10), one may calculate $\Phi(x,y,\theta)$ by integrating $\varphi(x,y,\theta)$ although stripe artifact caused by noise accumulation appears occasionally in a resultant image corresponding to $\Phi(x,y,\theta)$. However, it is also possible to reconstruct $\delta(X,y,Z)$ directly from $\varphi(x,y,\theta)$ as below.[11]

In tomographic algorithm,

$$\delta(X,y,Z) = \int_0^{\pi}\int_{-\infty}^{\infty} P(\omega,y,\theta)\exp\left[2\pi i\omega(X\cos\theta - Z\sin\theta)\right]|\omega|d\omega d\theta \tag{12}$$

is calculated, where $P(\omega,y,\theta)$ is the Fourier transform of experimental data (that is, $\Phi(x,y,\theta)\lambda/2\pi$ in this case). Here, it should be noted that the Fourier transform of $\varphi(x,y,\theta)$, $A(\omega,y,\theta)$, is given using $P(\omega,y,\theta)$ by

$$A(\omega,y,\theta) = 2\pi i\omega P(\omega,y,\theta). \tag{13}$$

Then, eq. (12) is rewritten as

$$\delta(X,y,Z) = \frac{1}{2\pi i}\int_0^{\pi}\int_{-\infty}^{\infty} A(\omega,y,\theta)\exp\left[2\pi i\omega(X\cos\theta - Z\sin\theta)\right]\mathrm{sgn}(\omega)d\omega d\theta, \tag{14}$$

where $\mathrm{sgn}(\omega)$ is the sign function

$$\mathrm{sgn}(\omega) = \begin{cases} 1 & \omega > 0, \\ -1 & \omega < 0. \end{cases} \tag{15}$$

Thus, $\varphi(x,y,\theta)$ can be used for the input data of filtered-backprojection method with $\mathrm{sgn}(\omega)/2\pi i$ as a filter function. Phase tomograms mapping the δ presented in the next Section were reconstructed with this approach.

3. BIOLOGICAL IMAGING WITH SYNCHROTRON RADIATION

An X-ray Talbot interferometer was constructed with a grating described above first at the beamline 20XU of SPring-8, Japan, where undulator radiation 245 m downstream from the source was available. The fundamental performance of the X-ray Talbot interferometer was reported previously[4]; the visibility of the generated moiré pattern was about 80% with the X-ray wavelength at 0.065 nm, and even at 0.03 nm, over 30% visibility was attained and tomographic imaging could be carried out.

A demonstration described in this paper was carried out at the beamline 20B2 of SPring-8, where a wide beam was available from a bending section. The effective area of the gratings (20 mm × 20 mm) was entirely illuminated by X-rays, and almost whole body imaging was performed for a fish (*Hasemania nana*) 3 cm in length. The fish was put in a cell filled with formalin, and placed just in front of the phase grating. The fish was rotated about the y axis with a step of 0.36° over 180°. $\varphi(x,y,\theta)$ was measured at every angular position of the sample rotation by the fringe scanning method with a $d/5$ step of displacement of the amplitude grating. Moiré patterns were recorded with a CCD camera (C4742-95HR, Hamamatsu Photonics) lens-coupled with a phosphor screen. Its effective pixel size was 11.8 μm × 11.8 μm. The exposure time for obtaining a moiré pattern was 8.2 s.

Figures 2 and 3 show reconstructed tomograms measured using 0.07-nm X-rays. Although some line artifacts arose from the surface and bone, organ structures were clearly revealed with bones in the same view. The line artifacts appear always at the region where the spatial change in the refractive index is prominent, in other words, where the beam deflection is comparatively large. This implies that $\varphi(x,y,\theta)$ is not determined correctly at clear structural boundaries within the assumption used in the formulation described above. In order to reduce the artifact, we need to reconsider eq. (2) or eq. (11); that is, the propagation of wavefront from the sample to the detector should be dealt with the theory of wave optics in the future.

Figure 4 shows the visibility of the moiré fringes observed at the beamline 20B2. Although the visibility decreased with increasing X-ray energy, the X-ray Talbot interferometer exhibited moiré fringes with a visibility sufficient for phase imaging at 0.04 nm. The fish sample was also observed with 0.045-nm X-rays, and images almost comparable to those by 0.07 nm X-rays were obtained, as shown in Fig. 5.

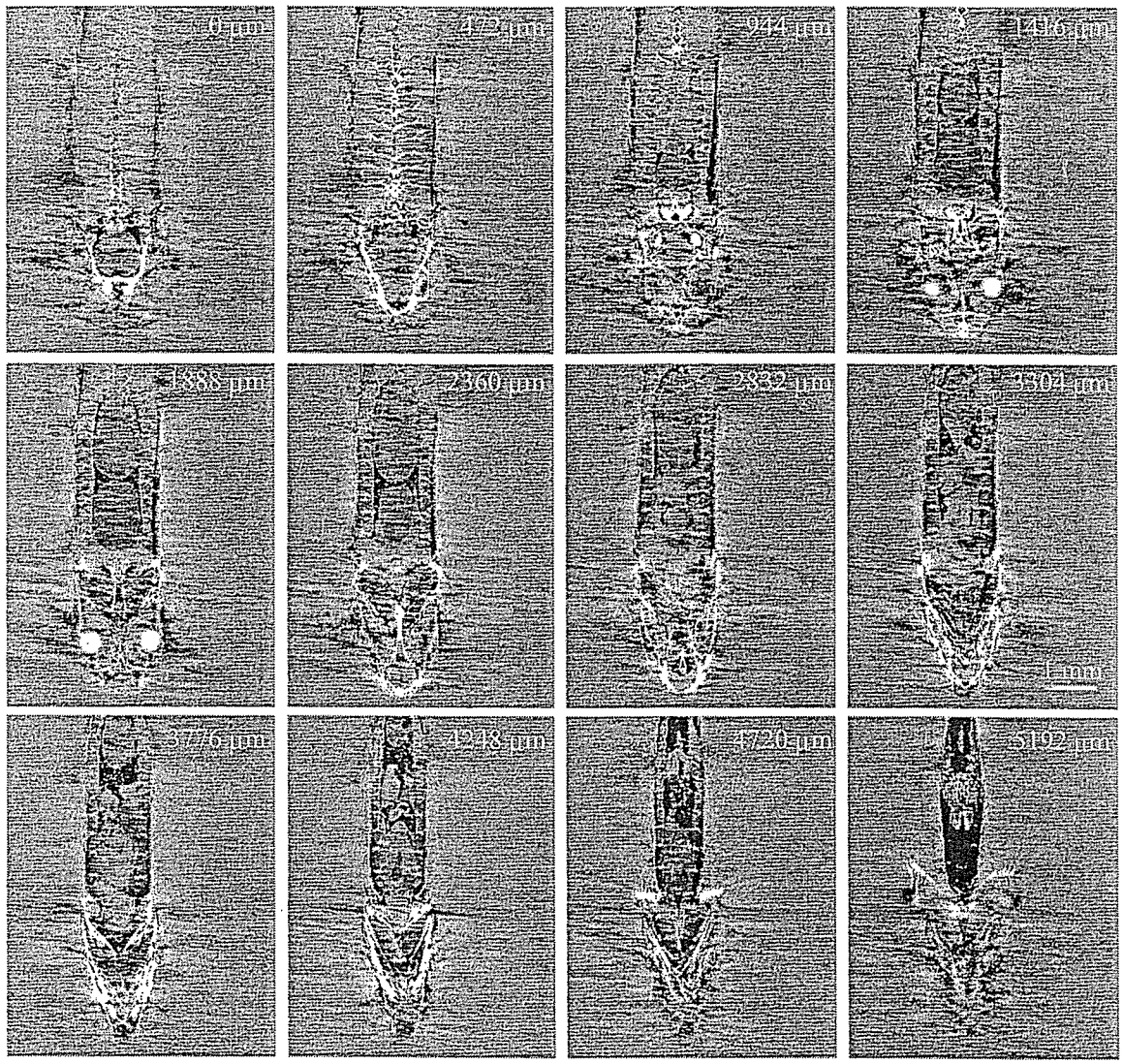

Figure 2. Phase tomograms (coronal views) of a fish (*Hasemania nana*) 3 cm in length from the back to the stomach. The relative positions of the tomograms are shown. X-ray wavelength was 0.07 nm.

4. PROSPECTS

4.1. Combination with an X-ray imaging microscope

The spatial resolution of X-ray phase imaging by Talbot interferometry is limited by the pitch of the grating. One approach for improving the spatial resolution is the reduction of the pitch. Another approach is the combination with X-ray imaging microscopy. X-ray imaging microscopes, which use focusing optics such as Fresnel zone plates, have been intensively developed using synchrotron X-rays. Because a Talbot interferometer functions for a spherical-wave X-rays because of using grating optics, the combination shown in Fig. 6 is feasible.

A preliminary experiment was carried out at the beamline 20XU of SPring-8, using a zone plate (ZP100-320-16, Xradia) whose outermost zone width, diameter, and gold-pattern thickness were 100 nm, 320 μm, and 1.6 μm, respectively. A sample was placed 339 mm upstream of the zone plate and a CCD-based X-ray image detector, whose effective pixel size was 3.14 μm, was set at the position 5.96 m from the zone plate. The focal length of the zone plate was 320 mm and the magnification of the system was 17.6. An amplitude grating 8

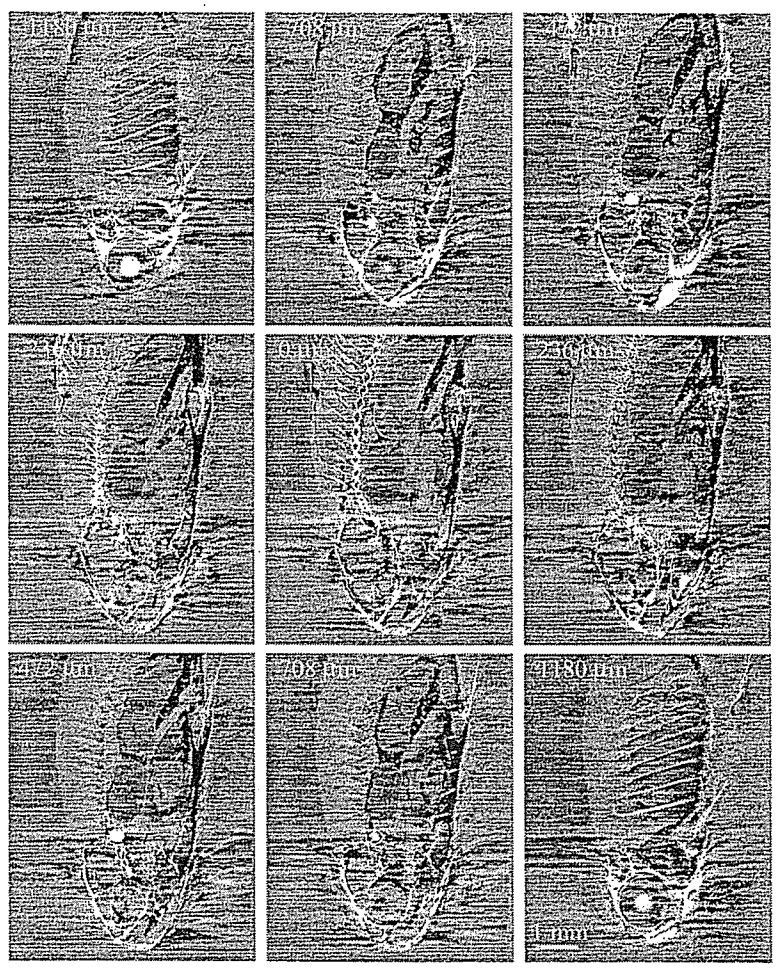

Figure 3. Phase tomograms (sagittal views) of a fish (*Hasemania nana*) 3 cm in length. The relative positions of the tomograms are shown. X-ray wavelength was 0.07 nm.

μm in pitch was placed just in front of the image detector and the phase grating 8 μm in pitch was set 339 mm upstream of the amplitude grating. The distance was calculated by

$$z = \left(\frac{1}{z_0} - \frac{1}{r} \right)^{-1}, \tag{16}$$

where z_0 is the distance in the case of plane-wave illumination given by eq. (6), and r is the distance from the focal point to the phase grating.

Figure 7(a) shows a resultant image obtained using 0.1 nm X-rays. We used a set of gratings used in the plane-wave experiment described above. Moiré fringes therefore appeared because the period of the self-image was enlarged to $d(r+z)/r$ which was mismatched with the pitch of the amplitude grating. The fringes were not crucial because their effect could be removed during the calculation of a differential phase map (Fig. 7(b)) by the fringe scanning method. A sample consisting of polystyrene spheres was used for this demonstration, which suggests that an X-ray Talbot interferometer, in other words an X-ray phase-sensitive detector, can be used to adapt a phase-contrast mode to X-ray imaging microscopes.

4.2. Combination with a compact X-ray source

The high sensitivity of X-ray phase imaging is attractive from a medical point of view. For practical applications, however, it is important to develop imaging systems outside huge synchrotron facilities. As mentioned, an X-ray

Talbot interferometer functions with spherical-wave (cone-beam) X-rays. Therefore, laboratory (or hospital) X-ray generators are available, provided that the spatial coherency is assured to be as high as needed for the operation of an X-ray Talbot interferometer. As discussed in the previous paper,[4] the spatial coherence length L given by

$$L = \frac{\lambda R}{2\pi\sigma_x}, \tag{17}$$

at the distance R from a source with a Gaussian intensity distribution $\exp\left(-x^2/2\sigma_x^2\right)$ should satisfy

$$L > d/3 \tag{18}$$

when a $\pi/2$ phase grating is used. We are now developing a phase grating of a pitch of 4.5 μm for a cone-beam X-ray Talbot interferometer, and in that case $\sigma_x < 4.2$ μm (10 μm FWHM) is needed when $R = 1$ m and $\lambda = 0.04$ nm. Because no restriction is put with respect to the spatial coherency in the y direction, a line focus is strictly available if the thickness of the line is smaller than the requirement.

Such an X-ray source is commercially available, but its flux is not high. Applications to non-destructive

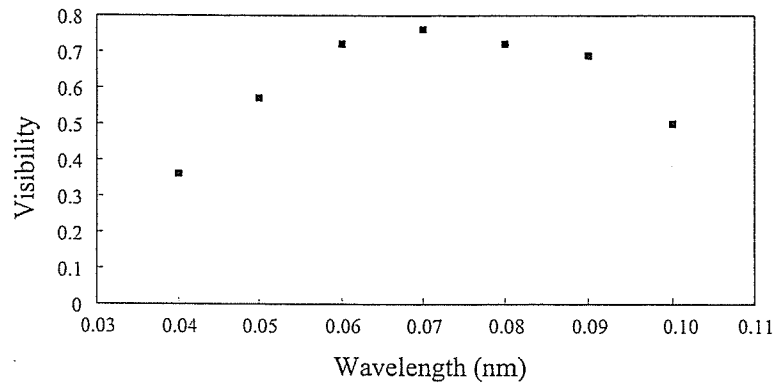

Figure 4. Visibility of moiré fringes generated by the X-ray Talbot interferometer as a function of X-ray wavelength.

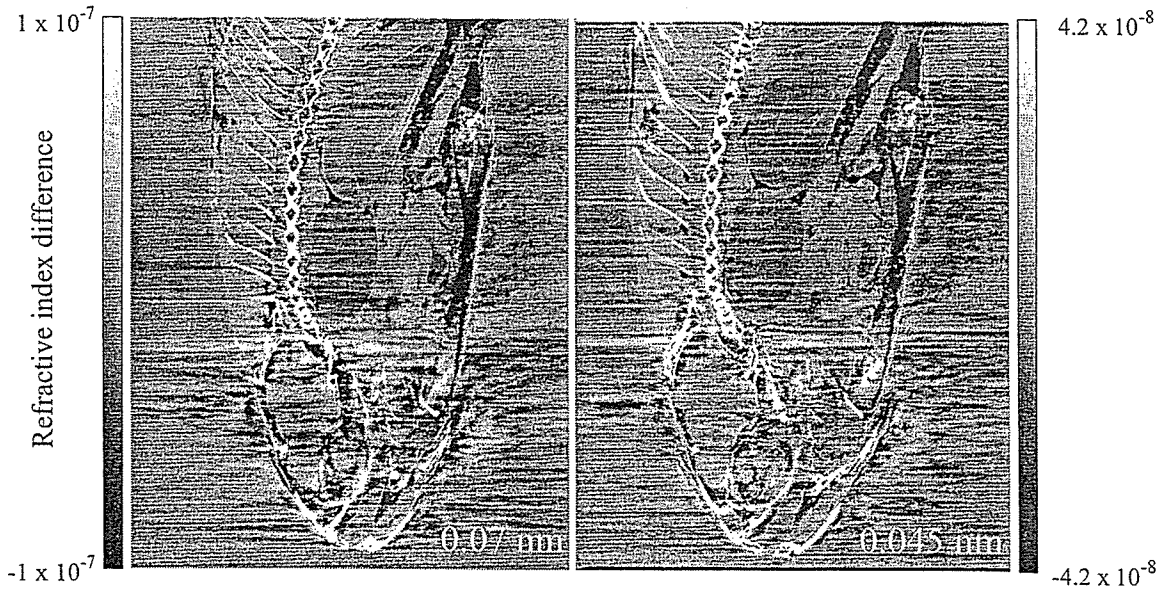

Figure 5. Comparison of the tomograms of the fish obtained with 0.07 nm and 0.045 nm X-rays.

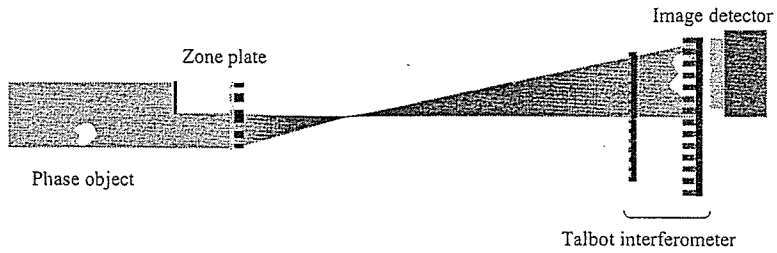

Figure 6. Phase-sensitive X-ray microscope attained by combining X-ray Talbot interferometer with X-ray imaging microscope.

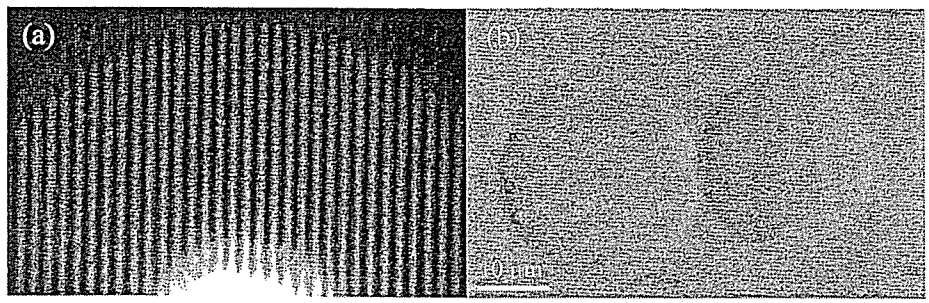

Figure 7. Result of Talbot-type X-ray imaging microscope; (a) moiré image and (b) differential phase map of polystyrene spheres.

observation that allow a long-time exposure may be feasible with such a source. However, radiologists do not accept a long-time exposure for clinical use. The development of high-flux microfocus X-ray generator is therefore required for practical application of X-ray Talbot interferometry.

Recently, X-ray Talbot-Lau interferometry has been demonstrated as an alternative approach, which employs a one-dimensional array of X-ray sources.[12] The size of the individual X-ray source corresponds to that required in X-ray Talbot interferometry. The period of the array d_0 is determined so that the self-images (period d) formed by the individual sources overlap with a displacement equal to the multiple of d; that is,

$$d_0 = \frac{R}{z} md, \qquad (m = 1, 2, \cdots) \tag{19}$$

where z is the distance from the grating to the self-image. It should be noted that coherency between individual sources is not needed. Practically the array is realized by using a multi-slit in combination with an X-ray source of a comparatively large focus. This approach allow us to use a conventional high-power X-ray source, and therefore X-ray Talbot-Lau interferometry is promising for clinical applications. (Because the use of the multi-slit implies the increase of the size of the entire source, one needs to compensate the decrease in the spatial resolution to some extent.)

However, it should be continued to develop thicker amplitude gratings so that higher-energy X-rays can be used. Mammography is normally performed by using X-rays of comparatively low energies from a Mo source. When X-ray phase information is available, we no longer need to be persistent to the energy region because a sufficient contrast can be obtained in the higher energy region where the reduction in X-ray dose is attained. As mentioned, our amplitude grating has a pattern 30 μm in height, and it functioned with X-rays up to 30 keV. Stacking such gratings may be a possible approach for attaining effectively a taller pattern; up to 40 keV will be used by stacking two.

A normal X-ray generator emits characteristic X-rays and continuous X-rays. Although characteristic X-rays are favorable for the operation of the Talbot interferometer, few target materials are available for generating characteristic X-rays in the energy range of 30-40 keV. Therefore, we need an option of using continuous X-rays.

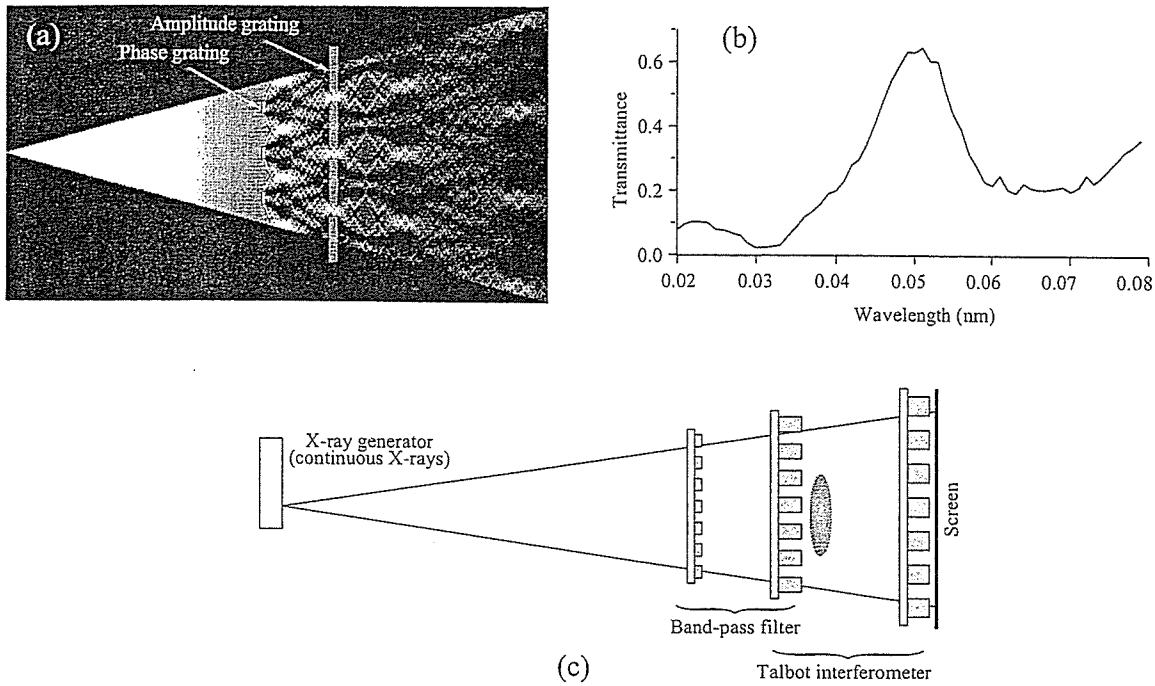

Figure 8. Band-pass filtering by fractional Talbot effect; (a) simulation of the X-ray intensity downstream of a π phase grating, and (b) spectral X-ray transmittance in the case that an amplitude grating is placed as shown in (a). (c) is an imaging setup with a continuous X-ray source and the band-pass filtering.

A Talbot interferometer functions with X-rays of a broad energy band because of using grating optics. In the previous paper,[4] it was estimated that a band width $\Delta E/E < 1/8$ is avaiable for X-ray Talbot interferometry. Monochromatization using a crystal, as normally adopted, is not suitable because the X-ray intensity would be reduced drastically.

Band-pass filtering for such a band width is attained by using the fractional Talbot effect. Figure 8(a) shows an intensity pattern downstream of a π phase grating of a 3:1 duty ratio. Remarkable concentration of the X-ray intensity is found at various positions from the grating. An amplitude grating is placed in one of such positions so that the concentrated X-rays can pass between the lines of the grating pattern. Here, it should be noted that the feature of Fig. 8(a) varies depending on X-ray energy. Therefore, this setting has a function of band-pass filtering. Figure 8(b) is a simulated spectral transmittance; thus, $\Delta E/E \sim 1/2$ is achieved. Because the spectrum of continuous X-rays has a cut-off on the high-energy side owing to the source operation condition and/or a filter and a reduction on the low-energy side owing to absorption by air and a filter, it will be able to tailor a spectrum suitable for an X-ray Talbot interferometer. As shown in Fig. 8(c), a third grating (amplitude type) is placed at the position that the fractional Talbot effect by the second grating occurs. Thus, the set of the first and second gratings functions as a band-pass filter and the set of the second and third gratings functions as a Talbot interferometer. In this case, a sample should be downstream of the second grating. Although it is possible to place the sample upstream of the second grating, one needs to accept some performance degradation of the band-pass filtering.

5. CONCLUSION

Phase tomography with an X-ray Talbot interferometer was performed for almost whole body three-dimensional imaging of a fish 3 cm in length. An amplitude grating of a gold pattern 8 μm pitch and 30 μm thick fabricated by X-ray lithography and electroplating was used to construct the Talbot interferometer. An X-ray Talbot interferometer has advantage that spherical-wave and/or polychromatic X-rays are available. A preliminary

operation of a phase-sensitive X-ray microscope by combining an X-ray Talbot interferometer with a normal X-ray imaging microscope was reported. Practical applications of X-ray Talbot interferometry with a conventional X-ray source is promising.

ACKNOWLEDGMENTS

The experiment using synchrotron radiation was performed under the approval of the SPring-8 committee 2006A1237-NM-np and 2006A1377. This study was financially supported by the project "Development of System and Technology for Advanced Measurement and Analysis" of Japan Science and Technology Agency (JST).

REFERENCES

1. A. Momose, S. Kawamoto, I. Koyama, Y. Hamaishi, K. Takai, and Y. Suzuki, "Demonstration of X-ray Talbot interferometry," *Jpn. J. Appl. Phys.* **42**, L866-L868 (2003).
2. T. Weitkamp, B. Nöhammer, A. Diaz, and C. David, "X-ray wavefront analysis and optics characterization with a grating interferometer," *Appl. Phys. Lett.* **86**, 054101 (2005).
3. T. Weitkamp, A. Daiz, C. David, F. Pfeiffer, M. Stampanoni, P. Cloetens, and E. Ziegler, "X-ray phase imaging with a grating interferometer," *Opt. Express* **13**, 6296-6304 (2005).
4. A. Momose, W. Yashiro, Y. Takeda, Y. Suzuki, and T. Hattori, "Phase tomography by X-ray Talbot interferometry for biological imaging," *Jpn. J. Appl. Phys.* **45**, 5254-5262 (2006).
5. S. Yokozeki and T. Suzuki, "Shearing interferometer using the grating as the beam splitter," *Appl. Opt.* **10**, 1575-1580 (1971).
6. A. W. Lohmann and D. E. Silva, "An interferometer based on the Talbot effect," *Opt. Commun.* **2**, 413-415 (1971).
7. A. Momose, S. Kawamoto, I. Koyama and Y. Suzuki, "Phase tomography using an X-ray Talbot interferometer," *SPIE Proc.* Vol. 5535, 352-360 (2004).
8. M. Matsumoto, K. Takiguchi, M. Tanaka, Y. Hunabiki, H. Takeda, A. Momose, Y. Utsumi, and T Hattori, "Fabrication of diffraction grating for X-ray Talbot interferometer," *High Aspect Ratio Micro Structure Technology Workshop* (2005) pp.22-23.
9. J. P. Guigay, "On Fresnel diffraction by one-dimensional periodic object, with application to structure determination of phase objects," *Opt. Acta* **18**, 677-682 (1971).
10. K. A. Stetson and W. R. Brohinsky, "Electrooptic holography and its application to hologram interferometry," *Appl. Opt.* **24** 3631-3637 (1985).
11. G. W. Faris and R. L. Byer, "Three-dimensional beam-deflection optical tomography of a supersonic jet," *Appl. Opt.* **27** 5202-5212 (1988).
12. F. Pfeiffer, T. Weitkamp, O. Buck, and C. David, "Phase retrieval and differential phase-contrast imaging with low-brilliance X-ray sources," *Nature Phys.* **2**, 258-261 (2006).

Japanese Journal of Applied Physics
Vol. 46, No. 3, 2007, pp. L89–L91

X-Ray Phase Imaging with Single Phase Grating

Yoshihiro TAKEDA, Wataru YASHIRO[1], Yoshio SUZUKI[2], Sadao AOKI, Tadashi HATTORI[3], and Atsushi MOMOSE[1]

Graduate School of Pure and Applied Sciences, University of Tsukuba, 1-1-1 Tennohdai, Tsukuba, Ibaraki 305-8573, Japan
[1]*Department of Advanced Materials Science, Graduate School of Frontier Sciences, The University of Tokyo, 5-1-5 Kashiwanoha, Kashiwa, Chiba 277-8561, Japan*
[2]*Japan Synchrotron Radiation Research Institute, SPring-8, 1-1-1 Kouto, Sayo, Hyogo 679-5198, Japan*
[3]*Laboratory of Advanced Science and Technology for Industry, University of Hyogo, 3-1-2 Kouto, Kamigori, Hyogo 678-1205, Japan*

(Received August 31, 2006; accepted November 1, 2006; published online January 12, 2007)

X-ray phase imaging with a single phase grating based on the fractional Talbot effect is described. A phase grating with an 8 μm pitch was placed behind a weakly absorbing object and illuminated with partially coherent 17.7 keV X-rays. Intensity patterns downstream of the grating were recorded with a high-resolution image detector. By the fringe scanning method, an X-ray wavefront inclination by the object was obtained. Phase tomography was performed and the three-dimensional structure of a piece of a polymer blend was revealed with an 8 μm spatial resolution and a 9 mg/cm^3 detection limit of density deviation.
[DOI: 10.1143/JJAP.46.L89]

KEYWORDS: X-ray imaging, phase measurement, Talbot effect, tomography, X-ray interferometer

Because of the penetrating power of X-rays, X-ray absorption imaging makes it possible to observe internal structures of objects nondestructively. However, it is difficult to depict weakly absorbing structures of an object consisting of light elements. When X-rays pass through an object, however, a considerably large phase shift occurs. Therefore, X-ray phase imaging that measures the distribution of an X-ray phase shift enables us to observe internal structures with high sensitivity. For X-ray phase imaging, many approaches were proposed and demonstrated in the middle of 1990s.[1–3]

Recently, X-ray phase imaging setups consisting of X-ray gratings have been reported.[4–8] Because these setups do not use crystal optics, it is possible to perform X-ray phase imaging with polychromatic and/or spherical-wave X-rays. When a phase grating is illuminated with partially coherent plane-wave X-rays, clear periodic intensity patterns whose periods correspond to the pitch of the grating appear at specific distances from the grating (fractional Talbot effect).[9–11] The pitch of the grating is chosen such that it is comparable to or smaller than the spatial coherence length of incident X-rays, usually below 10 μm. In these methods, the second grating, which should be absorption type, is overlaid on an intensity pattern, and the appearing moiré fringes whose spacings are much larger than the period of the intensity pattern are measured easily with a normal X-ray image detector. When a phase object is placed in front of the first grating, X-ray refraction at the objects causes the deformation of the periodic intensity pattern and therefore of the moiré fringes.

Note that we can omit the absorption grating if we can resolve the intensity pattern downstream of the first grating directly with an image detector. The X-ray fractional Talbot effect has been observed with a charge coupled devices (CCD) coupled with a scintillator and a coupling lens or an X-ray film.[4,5,12] For X-rays above 10 keV, the fabrication of an absorption grating is crucial because a pattern with an extremely high aspect ratio needs to be formed, which is not straightforward by normal lithographic techniques. Therefore, an approach that eliminates the use of an X-ray absorption grating and instead employs a high-spatial-resolution image detector is a good alternative. In addition, this approach opens up a new possibility for X-ray phase-sensitive microscopy.

In this paper, we describe an experimental demonstration of X-ray phase imaging with a single phase grating and a high-spatial-resolution image detector.

Let us consider a phase grating with a pitch d placed on the xy-plane ($z = 0$) so that the grooves of the grating are parallel to the y-axis. The complex transmission function of the grating $T(x)$ is expressed by a Fourier series expansion as

$$T(x) = \sum_n a_n \exp\left(2\pi i \frac{n}{d} x\right), \tag{1}$$

where a_n is the nth Fourier coefficient. When the grating is illuminated with unit-amplitude plane-wave X-rays whose wavelength is λ, the complex amplitude $E(x, y, z)$ of the X-rays downstream of the grating is also expressed by a Fourier series expansion as

$$\begin{aligned} E(x, y, z) &= \frac{1}{\sqrt{i\lambda z}} \int T(x_0) \exp\left[\frac{\pi i}{\lambda z}(x - x_0)^2\right] dx_0 \\ &= \sum_n b_n(z) \exp\left(2\pi i \frac{n}{d} x\right), \end{aligned} \tag{2}$$

with paraxial approximation,[13] where

$$b_n(z) \equiv a_n \exp\left(-\pi i \lambda z \frac{n^2}{d^2}\right). \tag{3}$$

Equations (2) and (3) indicate that the Fourier coefficient b_n varies along the optical axis (z-axis). The intensity distribution $I(x, y, z)$ is given by

$$\begin{aligned} I(x, y, z) &= |E(x, y, z)|^2 \\ &= \sum_n c_n(z) \exp\left(2\pi i \frac{n}{d} x\right), \end{aligned} \tag{4}$$

where

$$c_n(z) \equiv \sum_{n'} b_{n+n'}(z) b_{n'}^*(z). \tag{5}$$

At specific distances from the grating, clear periodic intensity patterns whose period is the same as that of the grating appear, as shown in Fig. 1, which is a calculated intensity distribution downstream of a $\pi/2$ shift phase grating.

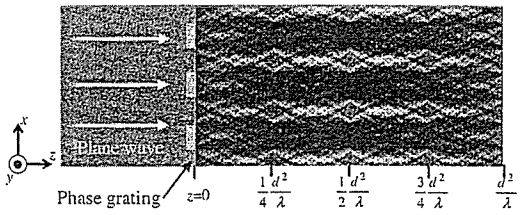

Fig. 1. Calculated intensity distribution caused by fractional Talbot effect downstream of $\pi/2$ phase grating.

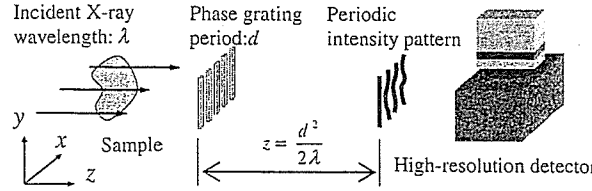

Fig. 2. Schematic diagram of experimental setup.

If an object is put in front of the grating, the X-ray wavefront is inclined by $\varphi(x, y)$ in the x-direction, which is given by

$$\varphi(x, y) = \frac{\lambda}{2\pi} \frac{\partial \Phi(x, y)}{\partial x}, \tag{6}$$

where $\Phi(x, y)$ is an X-ray phase shift at the object. When the grating is illuminated with such X-rays, the intensity distribution downstream of the grating $I(x, y, z)$ varies as

$$I(x, y, z) = \sum_n c_n(z) \exp\left\{2\pi i \frac{n}{d}[x - z\varphi(x, y)]\right\}. \tag{7}$$

This suggests that one can detect a phase object if the distortion of the periodic intensity pattern is resolved.

The measurement of $\varphi(x, y)$ is also attainable by the Fourier transform method or the fringe scanning method. By the Fourier transform method, the spatial resolution of the obtained image is limited by twice the period of the measured intensity pattern. On the other hand, there is no such problem by the fringe scanning method. Therefore, we used the fringe scanning method to determine $\varphi(x, y)$. When the phase grating is displaced by a distance kd/M along the x-direction, where k and M are integers, intensity distributions $I_k(x, y, z)$ given by

$$I_k(x, y, z) = \sum_n c_n(z) \exp\left\{2\pi i \frac{n}{d}\left[x - z\varphi(x, y) + \frac{d}{M}k\right]\right\}$$
$$k = 1, 2, \ldots, M \tag{8}$$

are observed. In the fringe scanning method, fringes with a sinusoidal profile are normally assumed. Higher orders ($n \geq 2$) in eq. (8) may cause error. However, by selecting an adequately large M, the error induced by the harmonics can be reduced.[14] We used a five-step fringe scan because the orders that cause the error are 4th, 6th, 9th, ...[5,8] The magnitudes of the 9th and higher orders are normally negligible; furthermore, the magnitudes of the even orders are negligible if the line : space of the grating is 1 : 1. Then, one can use

$$\frac{2\pi}{d}[x - z\varphi(x, y)] \approx \tan^{-1}\left(\frac{\sum_{k=1}^{5} I_k(x, y, z) \sin\left(2\pi\frac{k}{5}\right)}{\sum_{k=1}^{5} I_k(x, y, z) \cos\left(2\pi\frac{k}{5}\right)}\right). \tag{9}$$

The effect of the carrier fringe with a period d is removed by subtracting the value obtained by the fringe scanning method without an object from the value obtained with the object. Thus, the map of X-ray wavefront inclination $\varphi(x, y)$ and the differential phase map $\partial\Phi(x, y)/\partial x$ can be calculated. An X-ray phase shift map $\Phi(x, y)$ is obtained by integrating the differential phase map. A phase tomogram can be reconstructed using a conventional computed tomography (CT) algorithm from multiple phase maps measured at various angular positions of the sample rotation.

Figure 2 shows the experimental setup used at the beamline BL20XU of SPring-8, Japan. X-rays emitted from an undulator were monochromatized to 17.7 keV by a Si double-crystal monochromator. At a distance of 245 m from the source, a phase grating was placed so that the groove is parallel to the plumb line. We used a gold phase grating fabricated by UV lithography and electroplating. The pitch of the grating was 8 μm and its line : space was 1 : 1. The height of the pattern was 2 μm, which corresponds to the amount of $\pi/2$ phase shift for 17.7 keV X-rays. We used a CCD camera with a Ce-doped Lu_2SiO_5 scintillator and an optical coupling lens.[15] The effective pixel size was 1.0 μm and the field of view was about $1.3 \times 1.0\,mm^2$. The camera was placed at $z = 457$ mm and used to measure the periodic intensity pattern. The position was selected because the visibility of the pattern reaches 100% ideally at $z = d^2/2\lambda$ in the case of a $\pi/2$ shift phase grating.[10]

As a sample, a piece of polystyrene (PS)/poly(methyl methacrylate) (PMMA) polymer blend was placed in a cell filled with water, which was placed in front of the grating. The sample had structures consisting of PS-rich and PMMA-rich regions, which have been proved to be observable by Bonse–Hart-type X-ray interferometer.[16]

Figure 3(a) shows an intensity pattern obtained by exposing with X-rays for 1.5 s. An enlarged image of the area indicated by the broken-line box in Fig. 3(a) is shown in Fig. 3(b), where a distortion of the periodic intensity pattern is observed. Figure 3(c) shows a map of the X-ray wavefront inclination obtained from the intensity patterns using eq. (9). The sample was rotated in 2° steps over 180° and 90 phase maps were obtained.

Figure 4(a) shows an axial section of the reconstructed phase tomogram at the position of the dotted line in Fig. 3(c). A three-dimensional rendering view is shown in Fig. 4(b) where the PS-rich region is made transparent. A bicontinuous structure of the polymer blend is clearly shown in Figs. 4(a) and 4(b). The pixel values in the reconstructed phase tomogram indicate the refractive index difference between the object and the surrounding water.[1] The refractive index differences were 0.2×10^{-7} between the PS-rich region and water, and 1.1×10^{-7} between the PMMA-rich region and water. These values are consistent with the result of X-ray phase tomography obtained using a Bonse–Hart-type X-ray interferometer.[16] The detection limit of the refractive index deviation was evaluated to be 6.2×10^{-9} from the noise of the tomogram. This value is related to the

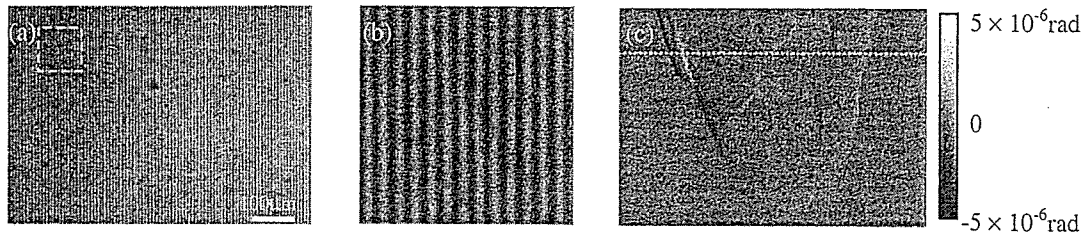

Fig. 3. (a) Intensity pattern distorted by piece of polymer blend. (b) Enlarged image of region indicated by broken-line box in (a). (c) Wavefront inclination map caused by refraction at object. In this figure, the X-ray wavefront inclined in one direction indicates a positive value and the wavefront inclined in the opposite direction indicates a negative value.

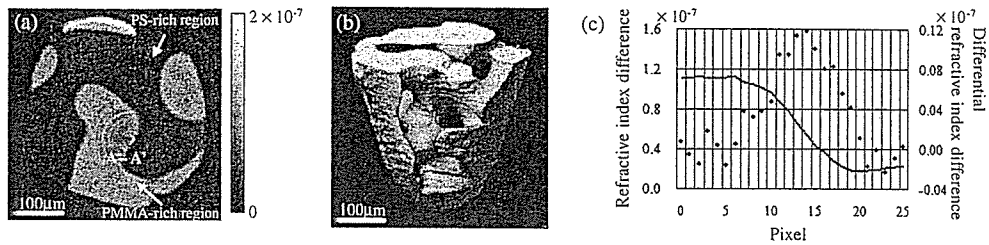

Fig. 4. (a) Axial section of reconstructed phase tomogram of piece of polymer blend. (b) Three-dimensional rendering view, in which PS-rich region is made transparent. (c) Evaluation of spatial resolution. The solid line and dots show the profile (left ordinate) and its differential (right ordinate) on line A–A′ in (a).

detection limit of the density deviation of 9 mg/cm^3 because the refractive index difference is approximately proportional to the density difference.

Figure 4(c) shows a profile across the boundary between the PS-rich and PMMA-rich regions indicated by A–A′ in Fig. 4(a) and its differential. The spatial resolution in the phase tomogram was evaluated to be 8 μm on the basis of the full-width at half maximum (FWHM) of the differential profile. There was a certain distance between the detector and the object using this method. Therefore, the blur caused by Fresnel diffraction was unavoidable. Because the distance was about 540 mm and the wavelength of the X-rays was 0.7 Å, the amount of the blur is estimated to be $\sqrt{\lambda z} = 6.1$ μm, which is considered as the factor that mainly influenced the spatial resolution. When the object is placed downstream of the grating, the periodic intensity pattern is deformed and the blur caused by the Fresnel diffraction is reduced. However, note that there is a trade-off relationship between spatial resolution and sensitivity because sensitivity is proportional to the distance between the object and the detector.

In this study, we succeeded in measuring the X-ray phase shift by placing a phase grating in front of a high-resolution detector. Thus, it is possible to append phase sensitivity to a conventional X-ray imaging setup in a simple manner. The proposed approach is also available with spherical-wave X-rays in an X-ray imaging microscope, avoiding the above-mentioned blur caused by Fresnel diffraction theoretically. If a phase grating is placed in an optical path of an X-ray microscope so that the periodic intensity pattern appears on the image plane, the X-ray phase shift at the object plane can be measured from the distortion of the intensity pattern. The combined use of an X-ray imaging microscope and the proposed method will lead to the development of a new type of differential phase X-ray microscope for quantitative analysis. We consider that such a combination is an important future research direction for the proposed method.

Acknowledgements

The experiment using synchrotron radiation was performed under the approval of the SPring-8 committee 2006A1237-NM-np. This study was financially supported by the project "Development of System and Technology for Advanced Measurement and Analysis" of the Japan Science and Technology Agency (JST).

1) A. Momose: Nucl. Instrum. Methods **352** (1995) 622.
2) T. J. Davis, D. Gao, T. E. Gureyev, A. W. Stevenson, and S. W. Wilkins: Nature **373** (1995) 595.
3) A. Snigirev, I. Snigireva, V. Kohn, S. Kuznetsiv, and I. Schelov: Rev. Sci. Instrum. **66** (1995) 5486.
4) A. Momose, S. Kawamoto, I. Koyama, Y. Hamaishi, K. Takai, and Y. Suzuki: Jpn. J. Appl. Phys. **42** (2003) L866.
5) A. Momose, S. Kawamoto, I. Koyama, and Y. Suzuki: Proc. SPIE **5535** (2004) 352.
6) T. Weitkamp, B. Nöhammer, A. Diaz, C. David, F. Pfeiffer, M. Stampanoni, P. Cloetens, and E. Ziegler: Appl. Phys. Lett. **86** (2005) 054101.
7) E. Pfeiffer, T. Weitkamp, O. Buck, and C. David: Nat. Phys. **2** (2006) 258.
8) A. Momose, W. Yashiro, Y. Takeda, Y. Suzuki, and T. Hattori: Jpn. J. Appl. Phys. **45** (2006) 5254.
9) J. M. Cowley and A. F. Moodie: Proc. Phys. Soc. B **76** (1960) 378.
10) J. P. Guigay: Opt. Acta **18** (1971) 677.
11) A. W. Lohmann and J. A. Thomas: Appl. Opt. **29** (1990) 4337.
12) P. Cloetens, J. P. Guigay, C. De Martino, J. Baruchel, and M. Schlenker: Opt. Lett. **22** (1997) 1059.
13) J. T. Winthrop and C. R. Worthington: J. Opt. Am. **55** (1965) 373.
14) K. A. Stetson and W. R. Brohinsky: Appl. Opt. **24** (1985) 3631.
15) H. Takano, Y. Suzuki, K. Uesugi, A. Takeuchi, and N. Yagi: Proc. SPIE **4499** (2001) 126.
16) A. Momose, A. Fujii, H. Kadowaki, and H. Jinnai: Macromolecules **38** (2005) 7197.

X-ray Phase Microtomography by Single Transmission Grating

Yoshihiro Takeda[1], Wataru Yashiro[2], Yoshio Suzuki[3] and Atsushi Momose[2]

[1]*Graduate School of Pure and Applied Sciences, University of Tsukuba, 1-1-1 Tennodai, Tsukuba, Ibaraki 305-8573, Japan*
[2]*Department of Advanced Materials, Graduate School of Frontier Sciences, The University of Tokyo, 5-1-5 Kashiwanoha, Kashiwa, Chiba 277-8561, Japan*
[3]*Japan Synchrotron Radiation Research Institute, SPring-8, 1-1-1 Kouto, Sayo-cho, Sayo-gun, Hyogo 679-5198, Japan*

Abstract. A preliminary experiment of X-ray phase microtomography by a single phase grating is reported. A phase grating was placed behind an object and illuminated by spatially coherent X-rays. At a specific distance from the grating, a periodic intensity pattern caused by the fractional Talbot effect was recorded with a high spatial-resolution image detector. A differential phase map related to the object was retrieved from the deformation in the periodic intensity pattern on the basis of the fringe scanning method. Phase tomograms of a piece of polymer blend were reconstructed and a phase-separation structure in the blend was successfully resolved.

Keywords: Phase, Tomography, Interferometer, Imaging, Grating
PACS: 07.05.Pj, 07.85.Tt, 41.50.+h. 42.25.Hz, 42.30.-d, 42.30.Rx, 42.30.Wb

INTRODUCTION

Because of the penetrating power of X-rays, X-ray absorption imaging makes it possible to observe internal structures of objects nondestructively. However, it is difficult to depict weakly absorbing structures in an object consisting of light elements. When X-rays pass through the object, however, quite a large phase shift occurs. Therefore X-ray phase imaging that measures the phase distribution of the X-rays, can realize high sensitive internal observation nondestructively.

Some methods for X-ray phase imaging was proposed in the middle of 1990s [1-3]. Recently, new X-ray interferometers consisting of X-ray gratings have been proposed and demonstrated [4-8]. The X-ray Talbot effect is used in the interferometers. When a grating is illuminated by spatially coherent X-rays, a periodic intensity pattern appears at a specific distance from the grating. In the X-ray Talbot interferometer [5], an absorption grating is overlaid on the periodic intensity pattern and generated moiré fringes are recorded. The pitch of the absorption gratings is made to be smaller than or comparable to the spatial coherence length of the incident X-rays. At the same time, it is required that the absorption grating is sufficiently thick to absorb the X-rays. This implies that a grating with a high aspect is required, but the fabrication of such a grating is not straightforward. On the other hand, the thickness of an X-ray phase grating can be much smaller than that of an absorption grating. Therefore it is comparatively easy to fabricate X-ray phase gratings. We propose a new method for X-ray phase imaging by a single phase grating that measures the periodic intensity pattern caused by the fractional Talbot effect with a high spatial-resolution detector instead of placing an amplitude grating on it.

PRINCIPLE

Figure 1 shows the experimental set up of the proposed method. A phase grating with a pitch d is placed on the x-y plane ($z = 0$) so that the grooves of the grating are parallel to the y axis. When the phase grating is illuminated by

CP879, *Synchrotron Radiation Instrumentation: Ninth International Conference*,
edited by Jae-Young Choi and Seungyu Rah

spatially coherent X-rays, a periodic intensity pattern appears at the downstream of the grating. Its intensity distribution $I(x,y,z)$ is written by

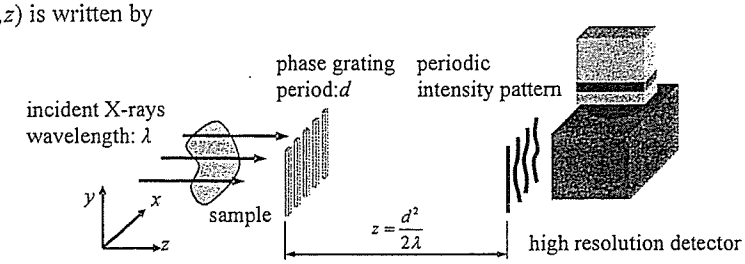

FIGURE 1. Experimental set up of the proposed technique.

$$I(x,y,z)=\sum_n b_n(z)\exp\left(2\pi i\frac{n}{d}x\right) \tag{1}$$

where $b_n(z)$ is the nth Fourier coefficient which depends on the complex transmission function of the phase grating. For a phase grating with a transmission function $T(x,y)=\exp[i\phi(x,y)]$, the periodic intensity pattern at $z = d^2/2\lambda$ is given by [9]

$$I\left(x,y,\frac{d^2}{2\lambda}\right)=1+\sin\left[\phi(x,y)-\phi\left(x+\frac{d}{2},y\right)\right] \tag{2}$$

In the case of a $\pi/2$ grating, the visibility of the pattern reaches 100% at $z = d^2/2\lambda$.

If an object with a phase shift $\Phi(x,y)$ is put in front of the grating, $I(x,y,z)$ is given by

$$I(x,y,z)=\sum_n b_n(z)\exp\left(2\pi i\frac{n}{d}\left[x-\frac{\lambda z}{2\pi}\frac{\partial\Phi(x,y)}{\partial x}\right]\right) \tag{3}$$

which indicates that the periodic intensity pattern is distorted by the object. A differential phase map $\partial\Phi(x,y)/\partial x$ can be retrieved by the Fourier transform method or the fringe scanning method from the deformed periodic intensity pattern. By the Fourier transform method, the spatial resolution of the retrieved image is limited by the pitch of carrier fringes; that is, the period of the pattern in this case. On the other hand, the fringe scanning method has no limit with respect to the period in principle, and therefore we adopted the fringe scanning methods.

When the phase grating is displaced by the distance kd/M along the x direction, where k is an integer, the intensity distribution is given by

$$I_k(x,y,z)=\sum_n b_n(z)\exp\left(2\pi i\frac{n}{d}\left[x-\frac{\lambda z}{2\pi}\frac{\partial\Phi(x,y)}{\partial x}+\frac{d}{M}k\right]\right) \tag{4}$$

In the fringe scanning method, the fringe of a sinusoidal profile is normally assumed. Higher orders ($n \geq 2$) in Eq. (4) are therefore the sources of error. However, by adequately selecting a large number for M, the error induced by the harmonics can be reduced [10]. We used 5-step fringe scan since the lowest order that causes error is 9th [7]. Because the magnitudes of such high orders are normally negligible, one can use a relation

$$2\pi\frac{n}{d}\left[x-\frac{\lambda z}{2\pi}\frac{\partial\Phi(x,y)}{\partial x}\right]\approx\arg\left(\frac{\sum_{k=1}^{5}I_k(x,y,z)\sin\left(2\pi\frac{k}{5}\right)}{\sum_{k=1}^{5}I_k(x,y,z)\cos\left(2\pi\frac{k}{5}\right)}\right). \quad (5)$$

to calculate a differential phase map $\partial\Phi(x,y)/\partial x$. An X-ray phase map is obtained through operations of unwrapping and integration on the differential phase map. A phase tomogram can be reconstructed from multiple phase maps measured at various angular positions of the sample rotation.

EXPERIMENT

The experiment was performed at BL20XU of SPring-8. X-rays emitted from an undulator was monochromatized to 17.7keV by a Si double-crystal monochromator. We used a phase grating with a gold pattern 8 μm in pitch and 2 μm in height fabricated by UV lithography and electro-plating. The pattern height corresponded to the amount for a $\pi/2$ phase shift. We used a CCD camera with a phosphor screen and a coupling lens. The effective pixel size was 1.0 μm and the field of view was about 1.3 mm × 1.0 mm. The camera was placed at $z = d^2/2\lambda$ and generated periodic intensity pattern was measured with it. In front of the grating, a piece of polystyrene (PS) / poly (methyl methacrylate) (PMMA) polymer blend was put as a sample. The sample had phase separation structures consisting of PS-rich phase and PMMA-rich phase. Figure 2(a) shows a periodic intensity pattern obtained by an exposure of 1.5 seconds. An enlarged image of the area indicated with broken lines in Fig. 2(a) is shown in Fig. 2(b), where the distortion of fringes is clearly seen. Five distorted patterns were measured by displacing the phase grating along the x direction by a one-fifth of the pitch. A differential phase map was calculated from the patterns, as shown in Fig. 2(c).

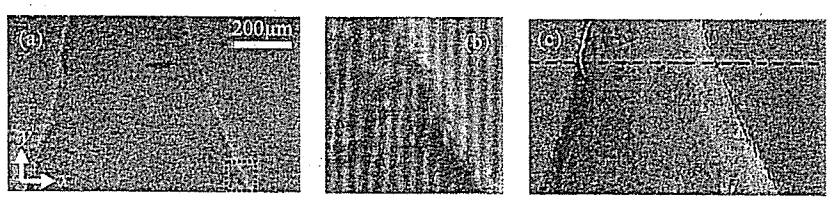

FIGURE 2. Distorted intensity pattern caused by a piece of polymer blend and calculated differential phase map. A close-up image of the region indicated by broken-line square in (a) is shown in (b). (c) is the differential phase map calculated on the basis of the fringe scanning method.

The sample was rotated in a 0.72-degree step over 180 degrees and 250 phase maps were obtained. Figure 3(a) shows a reconstructed phase tomogram at the position of the broken line in Fig. 2(c), and Fig. 3(b) shows a three-dimensional rendering view. The pixel values in reconstructed phase tomogram indicate the refractive index difference between the object and the surrounding air. The refractive index difference between the PS-rich phase and air was 7.5×10^{-7}, and between PMMA-rich phase and air was 8.5×10^{-7}. The detection limit of the refractive index deviation was evaluated to be 1×10^{-8} from the standard deviation of refractive index in the PMMA-rich phase. The spatial resolution in the phase tomogram was evaluated to be 7.5 μm by the FWHM of differential profile across the boundary between the PS-rich and PMMA-rich phases.

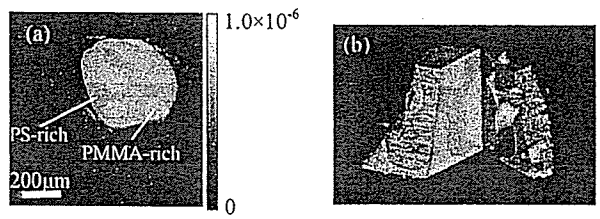

FIGURE 3. Reconstructed phase tomogram of a piece of polymer blend; (a) one of axial sections and (b) a three-dimensional rendering view, where the PS-rich region in the right-side part has been made transparent